Carbon 174 (2021) 325–334

Contents lists available at ScienceDirect

Carbon

journal homepage: www.elsevier.com/locate/carbon

Research Article

PVP-assisted synthesis of ultrafine transition metal oxides encapsulated in nitrogen-doped carbon nanofibers as robust and flexible anodes for sodium-ion batteries

Qingshan Zhao [1], Zhengzheng Xia [1], Tong Qian , Xianchao Rong , Mei Zhang , Yunfa Dong , Jinqing Chen , Hui Ning , Zhongtao Li , Han Hu , Mingbo Wu *

College of Chemical Engineering, College of New Energy, Institute of New Energy, State Key Laboratory of Heavy Oil Processing, China University of Petroleum (East China), Qingdao, 266580, China

ARTICLE INFO

Article history:
Received 17 September 2020
Received in revised form
6 December 2020
Accepted 6 December 2020
Available online 10 December 2020

Keywords:
Transition metal oxide
Electrospinning
Polyvinylpyrrolidone
Ultrafine
Sodium-ion battery

ABSTRACT

Transition metal oxides (TMOs) with high theoretical capacities are promising anode candidates for sodium ion batteries (SIBs), which yet suffers from inferior cycling stability and rate capability due to large volume change and sluggish transport kinetics during the sodiation/desodiation processes. Herein, a general strategy is developed to fabricate ultrafine TMOs nanoparticles encapsulated in nitrogen-doped carbon nanofibers (*uf*-TMOs@N-CNFs, M = Fe, Mn, Zn, etc.) as advanced anodes for SIBs. The *uf*-TMOs@N-CNFs are facilely synthesized via an in-situ electrospinning and subsequent carbonization strategy, among which polyvinylpyrrolidone (PVP) is employed as an effective dispersant to suppress metal agglomeration and control the size of TMOs. Benefiting from the intimate interaction between ultrafine TMOs and conductive N-CNFs substrates, the *uf*-TMOs@N-CNFs can efficiently mitigate the aggregation and pulverization of TMOs, facilitate electron/ion transfer, and boost pseudocapacitive charge storage, leading to superior sodium storage performance, including satisfactory reversible capacity, excellent rate capability, and durable cycling stability. Interestingly, the obtained *uf*-TMOs@N-CNFs membranes also exhibit excellent flexibility to serve as self-supported and flexible electrodes, demonstrating great potential for flexible SIBs. The present work provides a general and feasible method to construct robust and flexible electrodes for energy storage devices.

1. Introduction

With increasing concerns on the scarcity of lithium, sodium-ion batteries (SIBs) have received intensive attention as promising alternatives to lithium-ion batteries (LIBs) for the next-generation energy storage devices due to the abundant supply, low cost, and environmental friendliness of sodium resources [1,2]. In spite of similar electrochemical nature, traditional anodes for LIBs such as graphite cannot satisfy the demand of SIBs due to the larger ionic radius of sodium (Na^+: 1.02 Å *vs.* Li^+: 0.76 Å) [3,4], which causes lower transport/reaction kinetics and more serious volume expansion of the electrode [5]. To construct high-performance SIBs for practical applications, the development of efficient anode materials still remains a pressing challenge.

Owing to the high theoretical capacity and large natural abundance, transition metal oxides (TMOs) are considered as excellent anode candidates for SIBs. Unfortunately, the severe volume change during Na^+ insertion and extraction processes causes fracture and agglomeration of TMOs, resulting in the loss of mechanical strength and quick capacity fading. Meanwhile, the intrinsic low conductivity of TMOs and blocked electron transport restrict the improvement of rate performance. To solve these problems, two typical strategies can be expected from the amelioration of TMOs-based electrodes, including: i) nanosizing the particle, ii) compositing with carbon matrix [6–9]. Nanosizing the particle can efficiently decrease the absolute strain of TMOs during the sodiation/desodiation processes and thus improve the cycling stability. Enhanced rate capability can be also expected by shortening the electron diffusion length and enlarging the reaction-active area [10]. Another effective strategy is combination TMOs with conductive carbonaceous substrates, which can accommodate the volume expansion of TMOs and boost the electron transfer kinetics,

* Corresponding author.
E-mail address: wumb@upc.edu.cn (M. Wu).
[1] These authors contributed equally to this work.

https://doi.org/10.1016/j.carbon.2020.12.016
0008-6223/

leading to promoted sodium storage performance [11,12].

Recent efforts have demonstrated that merging nanosized TMOs with carbon nanomaterials can take advantages of the above two strategies together [13–19]. For instance, Kao et al. incorporated nanosized CuO nanoparticles (around 4 nm) into ordered mesoporous carbons through a hydrothermal and hydrogenation strategy [13]. The unique heterostructure can prevent the agglomeration of CuO and enhance Na^+ diffusion coefficients, delivering an excellent capacity of 477 mAh g^{-1} at 0.1 A g^{-1} after 200 cycles and 181 mAh g^{-1} at 2.0 A g^{-1} after 250 cycles. Mai and Zhang et al. fabricated ultrafine metal oxide dots (3–6 nm) embedded in nitrogen-enriched 3D carbon nanofiber networks via self-assembling of metal-polysaccharide frameworks and subsequent annealing, which showed superior electrochemical performance for lithium/sodium storage owing to the ultrasmall particle size and 3D carbon-confined structure [14]. Therefore, nanosized TMOs@carbon composites show great potential as advanced anode materials for high-performance SIBs. Nevertheless, incompact connection between TMOs and carbon matrices may limit the further improvement of energy storage performance, especially cycling stability at large current densities. Moreover, complicated procedure or high cost of nanosized TMOs@carbon impedes the scalable synthesis and practical applications. Therefore, feasible method for construction of versatile nanosized TMOs@carbon composites is still urgently desired.

In the present study, we demonstrate a general strategy to facilely and cost-effectively fabricate ultrafine TMOs nanoparticles encapsulated in nitrogen-doped carbon nanofibers (*uf*-TMOs@N-CNFs, M = Fe, Mn, Zn, etc.) through an in-situ electrospinning and subsequent carbonization strategy. In this process, polyvinylpyrrolidone (PVP) is employed as an effective additive to disperse the metal precursors and suppress metal agglomeration in the thermal treatment process. Owing to the ultrasmall size of TMOs and intimate integration with N-CNFs, the *uf*-TMOs@N-CNFs can efficiently mitigate aggregation and pulverization of TMOs, facilitate electron/ion transfer, and boost pseudocapacitive charge storage, leading to superior sodium storage performance, especially prominent rate capability and cycling stability. Interestingly, the versatile nanostructure of *uf*-TMOs@N-CNFs also endow them excellent flexibility and can be directly utilized as self-supported anodes for flexible SIBs.

2. Experimental section

2.1. Preparation of uf-TMOs@N-CNFs

In a typical synthesis process, 0.6 g polyvinylpyrrolidone (PVP, $M_W = 1300000$) and 3 mmol metal chloride ($FeCl_3$, $ZnCl_2$ or $MnCl_2$) were dissolved in 10 mL N, N-dimethylformamide (DMF) solution, followed by stirring for 2 h at 60 °C. Subsequently, 0.4 g polyacrylonitrile (PAN, $M_W = 150000$) was added into the mixture with vigorous stirring for 10 h at 60 °C to obtain a homogeneous precursor solution for electrospinning. The as-prepared solution was loaded into a plastic injector and electrospun on a spinning machine. A DC voltage of 14 kV was applied to the 20G needle of 0.6 mm inner diameter needles, and the flow rate was controlled at 0.006 mL min^{-1} during the spinning process. The distance between the tip and the collector wrapped aluminum foil (rotary speed of 300 r min^{-1}) was 12 cm to collect the as-spun fibers, which was directly scrapped off and carbonized at 600 °C for 2 h under a heating rate of 1 °C min^{-1} in nitrogen atmosphere. Finally, flexible membranes were obtained and denoted as *uf*-Fe_3O_4@N-CNFs, *uf*-ZnO@N-CNFs and *uf*-MnO@N-CNFs, respectively. In order to verify the crucial role of PVP, TMOs@N-CNFs (M = Fe, Zn and Mn) were synthesized through the same procedure in the absence of PVP.

2.2. Material characterization

The crystal structure of the samples was characterized with X-ray diffraction (XRD, X'Pert PRO MPD) using Cu Kα radiation (λ = 0.1518 nm) in angle of 2 theta from 5° to 75°. The morphology and microstructure were analyzed by scanning electron microscopy (SEM, Hitachi S-4800) and transmission electron microscopy (TEM, JEOL-2100F). The element mapping was recorded by energy dispersive X-ray spectroscopy (EDX) on the JEOL-2100F microscope operating at 200 kV. The X-ray photoelectron spectroscopy (XPS, Escalab 250Xi) analysis was conducted by an Mg Kα (1486.6 eV) monochromatic X-ray source. The thermal gravimetric analysis (TGA, STA 409 PC Luxx) was conducted in air with a heating rate of 10 °C min^{-1} at 800 °C. The N_2 adsorption-desorption isotherm measurement was obtained at 77 K on a sorptometer (Micromeritics, ASAP 2020). The specific surface area and pore volume were calculated using Brunauer-Emmett-Teller (BET) and Barrett-Joyner-Halenda (BJH), respectively. The inductively coupled plasma-atomic emission spectroscopy (ICP-AES) was conducted on AGILENT730ES.

2.3. Electrochemical measurements

The electrochemical performance was evaluated using CR2032-type coin cells, which were assembled in an Ar-filled glove box with water and oxygen contents <0.1 ppm at room temperature. The as-prepared *uf*-TMOs@N-CNFs were directly utilized as self-supported working anode for SIBs without any binder, conductive agent or current collector. The flexible membranes were punched into circular electrode slice (12 mm in diameter) as the test anode, with sodium metal as the counter electrode. The loading mass of *uf*-TMOs@N-CNFs and TMOs@N-CNFs were estimated about 1.0 mg cm^{-2}. Celgard 2300 membrane was utilized as the separator, and the electrolyte comprised 1 M $NaClO_4$ in a 2:1 (*v*/*v*) mixture of ethylene carbonate and propylene carbonate. The discharge and charge processes were tested on a LAND CT2001A battery test system over a voltage range of 0.01–3.00 V *vs*. Na/Na^+. The Nyquist impedance plots were performed at a frequency range of 100 kHz-10 MHz on an Ametek PARSTAT4000 electrochemistry workstation.

3. Results and discussion

3.1. Characterization and morphology

The *uf*-TMO@N-CNFs (M = Fe, Mn, Zn, etc.) composites were facilely prepared through an in-situ electrospinning and subsequent carbonization strategy (Fig. 1a). Specifically, metal chloride precursor and PVP dispersant were mixed and simultaneously added into polyacrylonitrile (PAN) spinning solution, which were electrospun into flexible nanofiber membranes, followed by one-pot carbonization. Ultrafine TMOs nanoparticles were homogenously encapsulated in nitrogen doped carbon nanofibers. On the contrary, TMOs@N-CNFs with uncontrollable larger TMOs particles were obtained without the addition of PVP. As illustrated in Fig. 1b, PVP is employed as a crucial additive in the synthesis process. Firstly, the negative charged O atoms in lactam groups of PVP show strong electrostatic affinity with M^{n+} ions, facilitating the homogeneous distribution of the metal precursors (Fig. S1) [20,21]. Additional experiments were carried out and further verify the intimate interaction between PVP and metal ions (Fig. S2). In subsequent thermal treatment process, the puissant PVP-bonded-M^{n+} interaction further contributes to suppress metal agglomeration and leads to controllable synthesis of ultrafine TMOs nanoparticles [22]. The speculative formation mechanism of TMOs is detailedly illustrated and listed in the supplementary information.

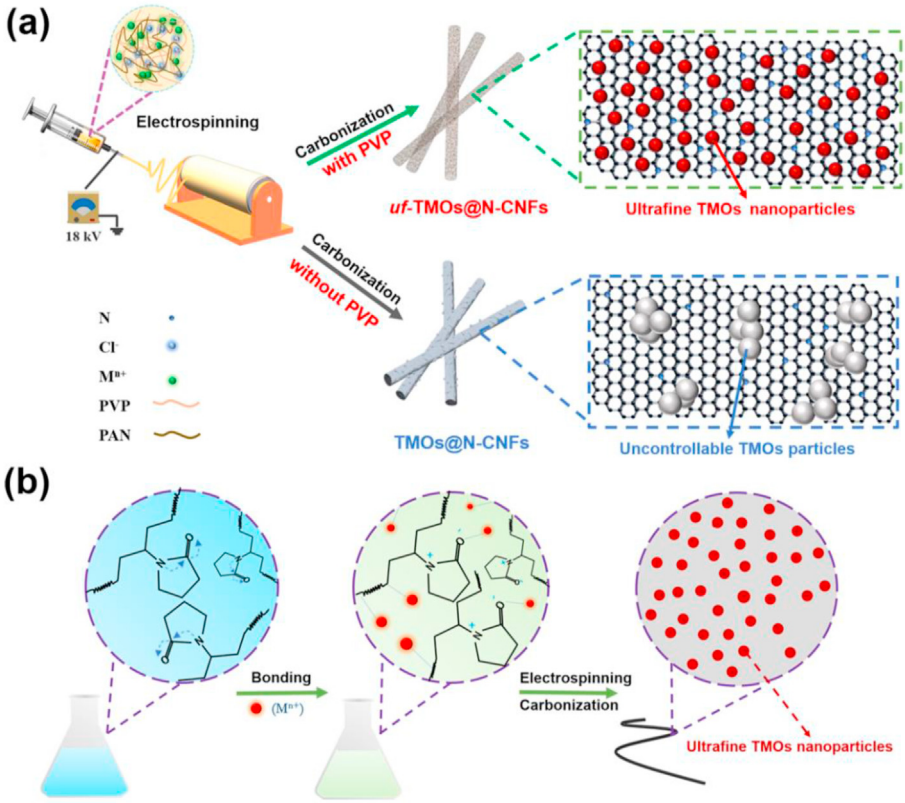

Fig. 1. (a) Schematic illustration for the synthetic process of *uf*-TMOs@N-CNFs and TMOs@N-CNFs. (b) Illustration for the PVP-assisted synthesis of ultrafine TMOs nanoparticles encapsulated in carbon nanofibers. (A colour version of this figure can be viewed online.)

Scanning electron microscopy (SEM) and transmission electron microscopy (TEM) images show the microstructure and morphology of the samples. As shown in Fig. S3, SEM images of *uf*-Fe_3O_4@N-CNFs display continuous carbon nanofibers with diameter ranging from 100 to 250 nm. Abundant cracks can be clearly observed on the surface of the nanofibers in the higher resolution SEM image (Fig. S3c). This is further supported by the nitrogen adsorption/desorption isotherms of *uf*-Fe3O4@N-CNFs, which exhibits a type IV isotherms with type H4 hysteresis loops, suggesting the existence of micropores and mesopores (Fig. S4) [23,24]. The BET surface area of *uf*-Fe_3O_4@N-CNFs is determined to be 78.73 $m^2\ g^{-1}$, and corresponding pore size distribution further confirms the plenty of micropores and mesopores. These cracks should be caused by gas evolution during the pyrolysis of PVP and PAN, which would be conducive to wetting of the electrolyte and transport of sodium ions [25]. Further study on the SEM and low-resolution TEM images reveals the absence of visible particles in the sample (Fig. 2a). Whereas magnified TEM images of *uf*-Fe_3O_4@N-CNFs indicate the existence of ultrafine nanoparticles (black dots) incorporated into the carbon nanofibers (Fig. 2b and inset). According to the size distribution analysis, the nanoparticles show a uniform size distribution with an average particle size of 3.7 nm (Fig. S5). As shown in Fig. 2c, the high-resolution TEM image further provides insights of ultrafine nanoparticles of well-crystalline texture with lattice fringe space of 0.253 nm, corresponding to the (311) plane of Fe_3O_4 [26]. As a control, in the absence of PVP, Fe_3O_4@N-CNFs presents uncontrollable larger particles with diameter of 15–45 nm supported on the surface of the nanofibers (Fig. 2d). In addition, dark field TEM image and corresponding energy dispersive X-ray spectroscopy (EDX) elemental mappings exhibit the homogeneous distribution of C, N, O and Fe elements in the *uf*-Fe_3O_4@N-CNFs (Fig. 2e and f).

To verify the universality of the PVP-assisted synthesis approach, the strategy was extended to other metal precursors such as $ZnCl_2$ and $MnCl_2$. The microstructures of the as-prepared *uf*-ZnO@N-CNFs and *uf*-MnO@N-CNFs were firstly characterized by TEM techniques (Fig. 3a and b). It can be clearly seen that no obvious agglomerated particles appear on the nanofibers, in line with that of *uf*-Fe_3O_4@N-CNFs. Magnified TEM images (insets of Fig. 3a and b) demonstrate the emergence of ultrafine nanoparticles uniformly dispersed in the samples. X-ray photoelectron spectroscopy (XPS) results further reveal that the ultrafine nanoparticles are supposed to be ZnO and MnO, respectively (Fig. S6 and Fig. S7). For comparison, ZnO@N-CNFs and MnO@N-CNFs prepared without PVP display irregular large particles (15–75 nm) on the surface of the nanofibers (Fig. 3c and d). The results demonstrate that PVP serves as an effective additive to control the size and distribution of TMOs, which should be attributed to its strong interaction with the metal precursors to prevent metal agglomeration and control formation kinetics of TMOs. Hence, a feasible and general method is successfully proposed for the fabrication of ultrafine TMOs nanoparticles intimately encapsulated in carbon nanofibers. Based on this, the metal loadings of *uf*-TMOs@N-CNFs were tested by inductively coupled plasma-atomic emission spectrometry (ICP-AES), as listed in Table S1. The mass ratios of Fe, Mn and Zn are determined to be 17.87 wt%, 18.07 wt% and 17.01 wt%, respectively. Accordingly, the mass percentage of Fe_3O_4, MnO and ZnO in the *uf*-TMOs@N-CNFs composites are calculated to be 24.68 wt%, 23.31 wt%, and 21.18 wt%, respectively.

As shown in Fig. 4a, the X-ray diffraction (XRD) patterns of *uf*-Fe_3O_4@N-CNFs and Fe_3O_4@N-CNFs display representative peaks of Fe_3O_4 (JCPDS 75–0033) without any second phase. A contrastive

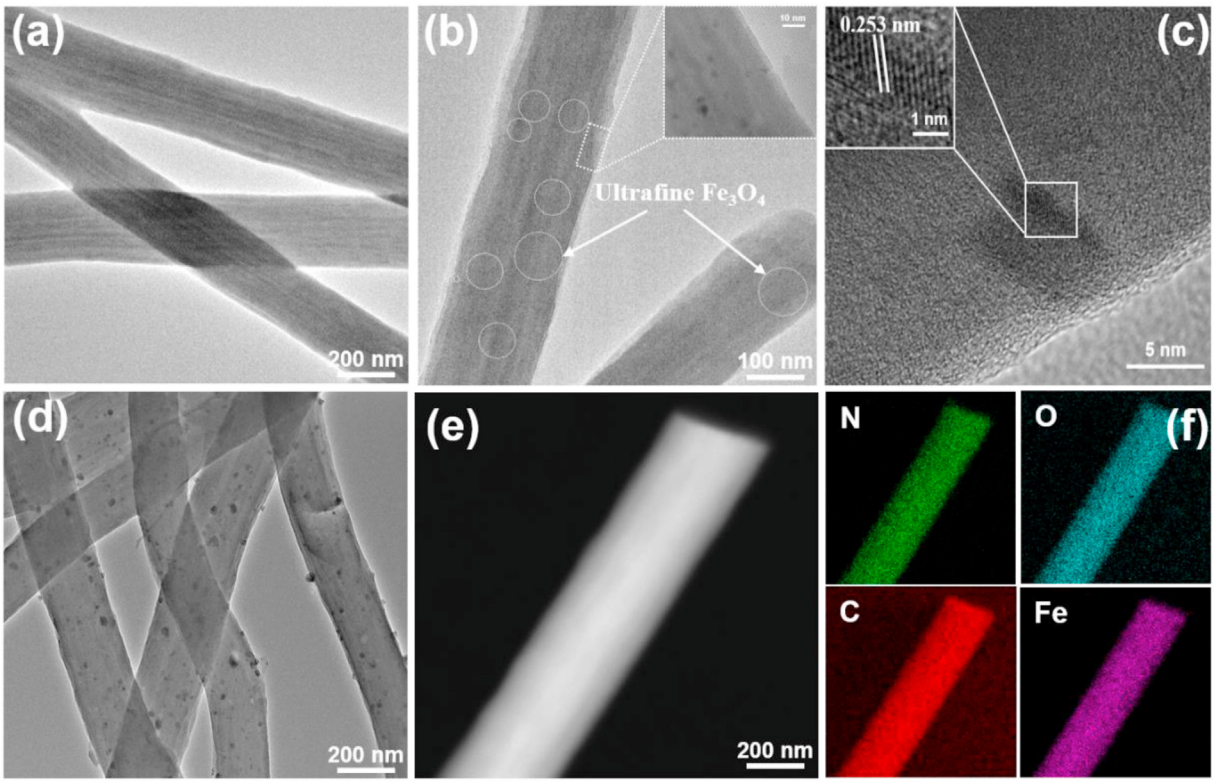

Fig. 2. TEM images of (a–c) *uf*-Fe_3O_4@N-CNFs and (d) Fe_3O_4@N-CNFs. (e) Dark-field TEM image and (f) corresponding EDX elemental mappings of *uf*-Fe_3O_4@N-CNFs with C, N, O and Fe element. (A colour version of this figure can be viewed online.)

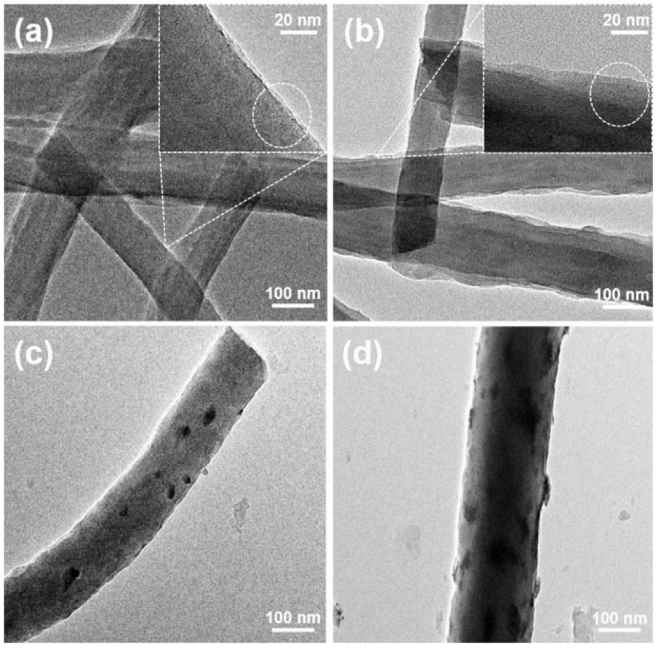

Fig. 3. TEM images of (a) *uf*-ZnO@N-CNFs, (b) *uf*-MnO@N-CNFs, (c) ZnO@N-CNFs and (d) MnO@N-CNFs.

study of the XRD patterns reveals broader diffraction peaks of *uf*-Fe_3O_4@N-CNFs than those of Fe_3O_4@N-CNFs, simultaneously with relative shifts to lower angles. The enlarged weak peaks of *uf*-Fe_3O_4@N-CNFs indicates a high dispersion of nano magnetite in the sample [27]. According to the Scherrer's equation, the calculated average crystallite sizes $\overline{D}$ of Fe_3O_4 in *uf*-Fe_3O_4@N-CNFs is about 4 nm (Table S2), which is in good agreement with the above TEM and size distribution analysis results. While the shifts to lower angles should be mainly assigned to tensile and compressive strains of the sample, resulting from their intimate interaction between ultrafine Fe_3O_4 and N-CNFs substrate [28–30]. Thermal gravimetric analysis (TGA) was conducted in air to determine the Fe_3O_4 content in the composite (Fig. 4b). With the temperature increasing, the sample starts to lose weight and shows a sharp decline from 380 to 410 °C due to the combustion of carbon and conversion of Fe_3O_4 to Fe_2O_3 (30.50 wt%). Accordingly, the mass percentage of Fe_3O_4 in *uf*-Fe_3O_4@N-CNFs is estimated to be 29.48 wt%, which is close to the ICP-AES testing value.

XPS spectra were further employed to characterize the surface compositions and chemical valence states of various elements in *uf*-Fe_3O_4@N-CNFs. The XPS survey spectrum confirms the existence of elemental C, N, O, and Fe in the sample (Fig. 5a). It is worth noting that the Fe content is detected to be 2.25 atomic% and corresponds to a Fe_3O_4 weight ratio of 12.41%, showing a difference with the TGA result. As we known, the depth range of XPS measurement is a nanometer order. Thus, the result should be assigned to the embedment of ultrafine Fe_3O_4 nanoparticles into the carbon nanofibers [31]. Additionally, with a doping amount of about 5.5 atomic% derived from PAN, nitrogen doping can further improve the electronic conductivity of the matrix [32]. The Fe 2p spectrum exhibits two broad peaks of Fe $2p^{3/2}$ at 710.1 eV and Fe $2p^{1/2}$ at 723.6 eV, which is consistent with previous reports (Fig. 5b) [33,34]. The characteristic satellite peaks of Fe 2p at 718.4 and 732.4 eV further confirms the formation of Fe_3O_4 [17,35]. Fig. 5c and d shows the existence of C–O/C=O (532.8 eV), which is resulted from the partial oxygen doping to carbon nanofibers originated from PVP [22]. Interesting, the presence of Fe–O–C bonds located at 531.8 eV,

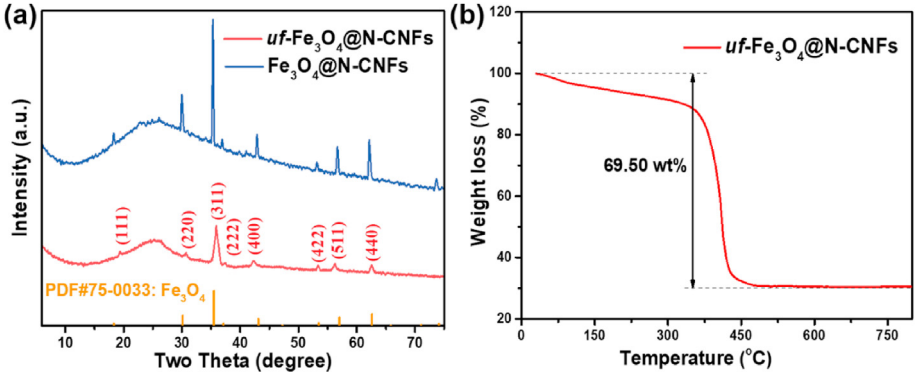

Fig. 4. (a) XRD patterns of *uf*-Fe_3O_4@N-CNFs and Fe_3O_4@N-CNFs. (b) TGA curve of *uf*-Fe_3O_4@N-CNFs. (A colour version of this figure can be viewed online.)

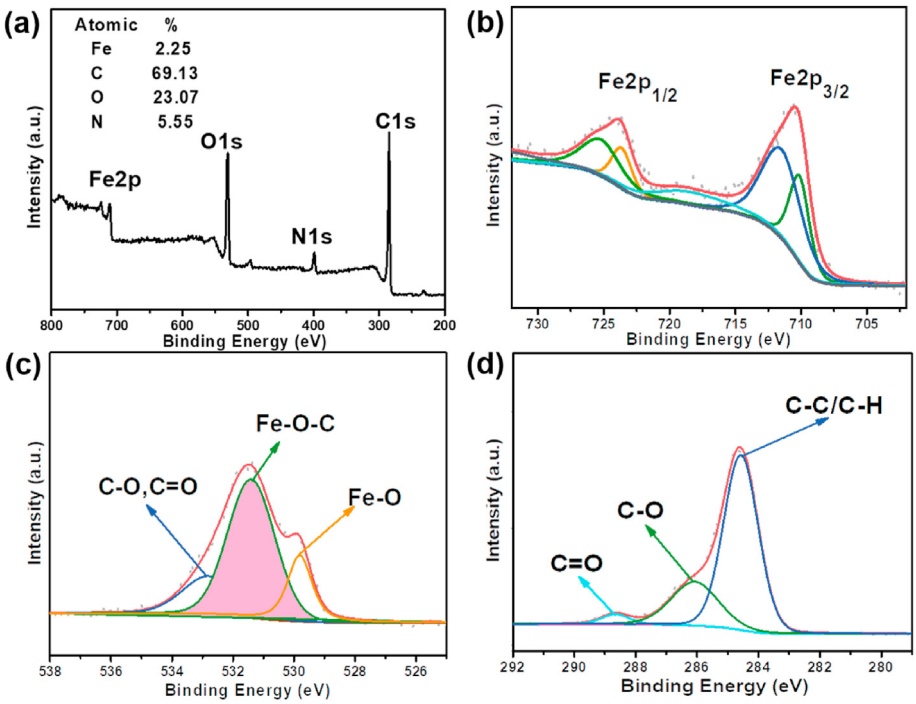

Fig. 5. (a) XPS survey, (b) Fe 2p, (c) O 1s and (d) C 1s spectra of *uf*-Fe_3O_4@N-CNFs. (A colour version of this figure can be viewed online.)

which is formed in the in-situ synthesis procedure of *uf*-Fe_3O_4@N-CNFs, demonstrates the strong chemical bonding between Fe_3O_4 and N-CNFs (Fig. 5c) [36,37]. Such intimate interaction between Fe_3O_4 and the carbonaceous substrate can effectively enhance the electron transfer and buffer the stresses arising from volume change of Fe_3O_4 in the sodiation/desodiation processes, leading to improved electrochemical properties [38,39]. To sum up, with the assistance of PVP, ultrafine TMOs with homogeneous particle size and distribution are intimately encapsulated in the N-CNFs matrix, which is expected to achieve exciting electrochemical performance when employed as anodes for sodium storage.

As shown in Fig. S8, the prepared *uf*-Fe_3O_4@N-CNFs, *uf*-ZnO@N-CNFs, and *uf*-MnO@N-CNFs membranes show excellent mechanical strength and can be directly tailored into working electrodes as self-supported anodes for SIBs without any binder, conductive agent or current collector. Therefore, coin-type 2032 half-cells were assembled to evaluate the electrochemical properties of the *uf*-TMOs@N-CNFs composites. The cyclic voltammetry (CV) curves of *uf*-Fe_3O_4@N-CNFs at 0.2 mV s^{-1} are shown in Fig. 6a. In the first cycle, the broad cathodic peak centered at 0.37 V is attributed to the irreversible electrolyte decomposition and solid electrolyte interphase (SEI) film formation, as well as the reduction of Fe_3O_4 to Fe^0 [40]. In the anodic process, the weak peak around 1.02 V indicates the oxidation of Fe^0 to Fe_3O_4 [27]. In the following anodic processes, the weak oxidization peaks at 0.76 V and 1.40 V corresponds to the two-step oxidation of Fe^0 to Fe^{2+} and Fe^{2+} to Fe^{3+}, respectively [36]. And reduction peaks at 0.66 V corresponds to the reduction of Fe^{3+}/Fe^{2+} to Fe^0 species. To further elucidate the conversion mechanism of iron species, *ex situ* XPS analyses of the *uf*-Fe_3O_4@N-CNFs electrodes at different charge/discharge stages were performed. As shown in Fig. S9. The pristine electrode displays four peaks of Fe^{3+} $2p_{3/2}$ (711.5 eV), Fe^{3+} $2p_{1/2}$ (725.2 eV), Fe^{2+} $2p_{3/2}$ (710.1 eV), and Fe^{2+} $2p_{1/2}$ (723.6 eV), respectively, corresponding to Fe_3O_4 [41]. When discharged to 0.8 V, the Fe^{3+} peaks at 711.5 and 725.2 eV are weakened and translated to Fe^{2+} peaks. After further discharge to 0.01 V, peaks of Fe^0 $2p_{3/2}$ (707.0 eV) and Fe^0 $2p_{1/2}$ (718.2 eV) generally emerged, indicating the reduction of Fe^{2+} to generate Fe^0 species [36,37]. Notably, the nanoscale Fe^0 species on the nanofiber

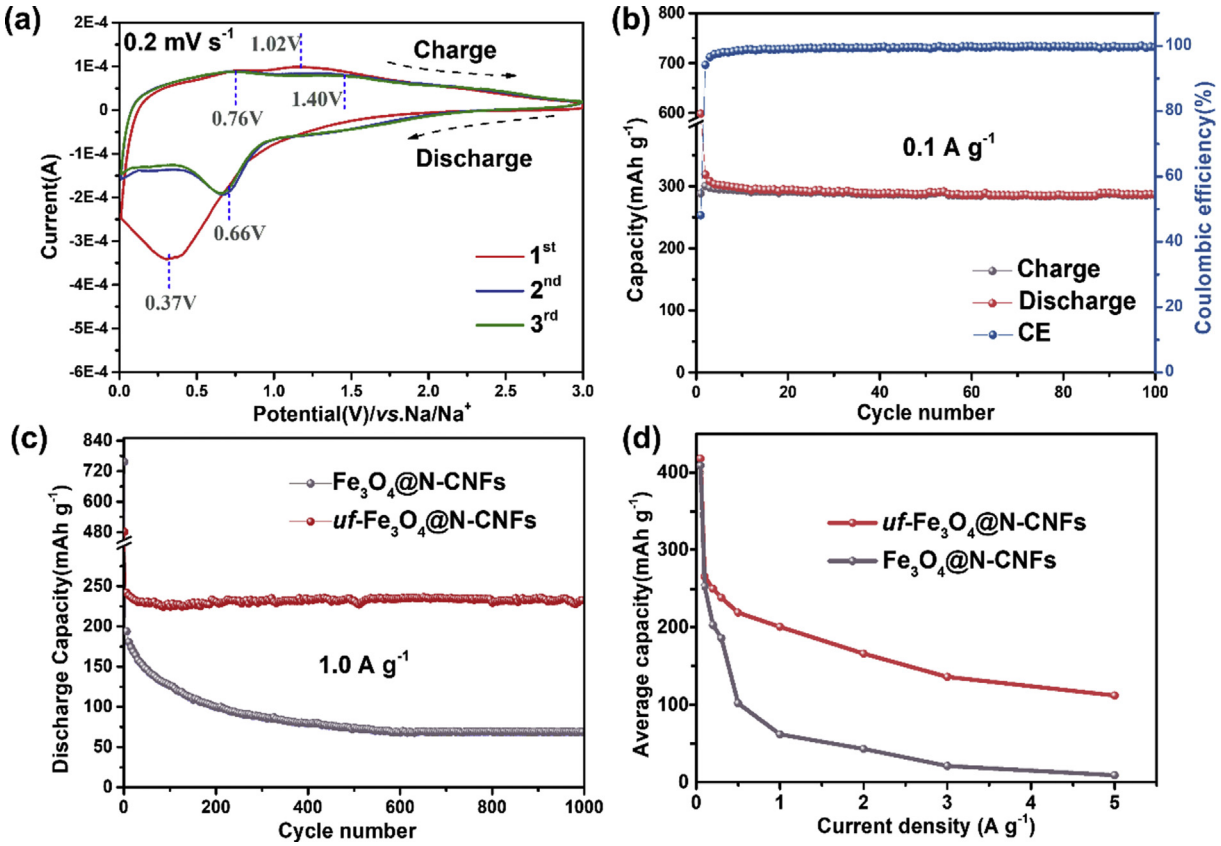

Fig. 6. (a) CV curves of *uf*-Fe_3O_4@N-CNFs at 0.2 mV s^{-1}. (b) Cycling performance of *uf*-Fe_3O_4@N-CNFs at 0.1 A g^{-1}. (c) Cycling performances of *uf*-Fe_3O_4@N-CNFs and Fe_3O_4@N-CNFs at 1.0 A g^{-1}. (d) The comparison of average capacity of *uf*-Fe_3O_4@N-CNFs and Fe_3O_4@N-CNFs at 0.05, 0.1, 0.3, 0.5, 1.0, 2.0, 3.0, and 5.0 A g^{-1}, respectively. (A colour version of this figure can be viewed online.)

surface are extremely active, which can be readily oxidized to Fe_2O_3 during the sample preparation and testing processes. Therefore, dominant Fe^{3+} peaks can also be observed in the XPS spectrum. When further charged to 1.8 and 3.0 V, the peaks of Fe^0 disappear and completely convert to Fe^{3+} peaks, demonstrating the reoxidation of Fe^0 to Fe^{3+}. Therefore, the CV and *ex situ* XPS results reveal the reversible redox conversion of iron species in the charge and discharge processes. Fig. 6b presents the cycling performance of *uf*-Fe_3O_4@N-CNFs at a current density of 0.1 A g^{-1}. The electrode delivers a capacity of 598 mA h g^{-1} with an initial coulombic efficiency (CE) of 48% on account of the decomposition of electrolyte and irreversible formation of SEI layer on the nanocomposite surface. After few cycles, the CE quickly rises to above 99%, and a stable charge capacity of 284 mA h g^{-1} remains after 100 cycles. When the current density is further raised to 1.0 A g^{-1}, *uf*-Fe_3O_4@N-CNFs affords a satisfactory and stable capacity of 235 mA h g^{-1} after 1000 cycles (Fig. 6c). In contrast, Fe_3O_4@N-CNFs suffers a severer capacity fading and shows a poor capacity of 77 mA h g^{-1} at the 1000th cycle.

Fig. 6d gives a comprehensive comparison of the average capacity of *uf*-Fe_3O_4@N-CNFs and Fe_3O_4@N-CNFs at different current densities. Owing to the prominent heterostructure, *uf*-Fe_3O_4@N-CNFs obviously displays superior sodium storage performance than that of Fe_3O_4@N-CNFs. Similar results can also be observed for *uf*-ZnO@N-CNFs and *uf*-MnO@N-CNFs. As shown in Fig. S10, the cycling performances of *uf*-MnO@N-CNFs and *uf*-ZnO@N-CNFs were evaluated, the results of which approve the good capacity and stable cyclability, delivering a high reversible capacity of 216 and 209 mA h g^{-1} after 1000 cycles, respectively. Whereas ZnO@N-CNFs and MnO@N-CNFs both show a rapid capacity fading in the first few cycles and presents a low capacity of 108 and 79 mA h g^{-1} after 400 cycles, respectively. The results reveal that the designed *uf*-TMO@N-CNFs demonstrate superior sodium storage performances owing to the distinctive composite nanostructure induced by the addition of PVP. Since the theoretical capacities of Fe_3O_4, MnO, and ZnO are 926, 755, and 978 mAh g^{-1}, respectively [42–44], and N-CNFs provides a capacity of 143 mAh g^{-1} at 0.1A g^{-1} according to the testing result in Fig. S11. Thus, the theoretical capacities of *uf*-Fe_3O_4@N-CNFs, *uf*-MnO@N-CNFs and *uf*-ZnO@N-CNFs are calculated by the equation of $C_{uf\text{-TMOs@N-CNFs}} = C_{TMOs} \times \%_{mass\ of\ TMOs} + C_{N\text{-CNFs}} \times \%_{mass\ of\ N\text{-CNFs}}$ [45], which are determined to be 336, 285, and 319 mAh g^{-1}, respectively (details listed in Table S3). Remarkably, the prepared *uf*-Fe_3O_4@N-CNFs, *uf*-MnO@N-CNFs and *uf*-ZnO@N-CNFs deliver capacities of 284, 271, and 304 mAh g^{-1} at a current density of 0.1A g^{-1}, which are extremely close to their theoretical capacities, taking full advantage of the intercalated TMOs. Tables S4–S6 present the performance of recent reported carbon-based Fe_3O_4, ZnO, and MnO composite anodes for SIBs. Comparison study reveals that the *uf*-TMOs@N-CNFs composites display superior capacity and stability, especially at large current densities.

Fig. 7a presents the rate capability of *uf*-Fe_3O_4@N-CNFs at different current densities. As can be seen, *uf*-Fe_3O_4@N-CNFs delivers average capacities of 308, 284, 268, 257, 240, 227, 180, 146, and 113 mA h g^{-1} at 0.05, 0.1, 0.2, 0.3, 0.5, 1.0, 3.0, and 5.0 A g^{-1}, respectively. When the current rate is reversed back to 0.1 A g^{-1}, the electrode capacity quickly recovers to 285 mA h g^{-1}, indicating an excellent rate performance of the electrode. The galvanostatic

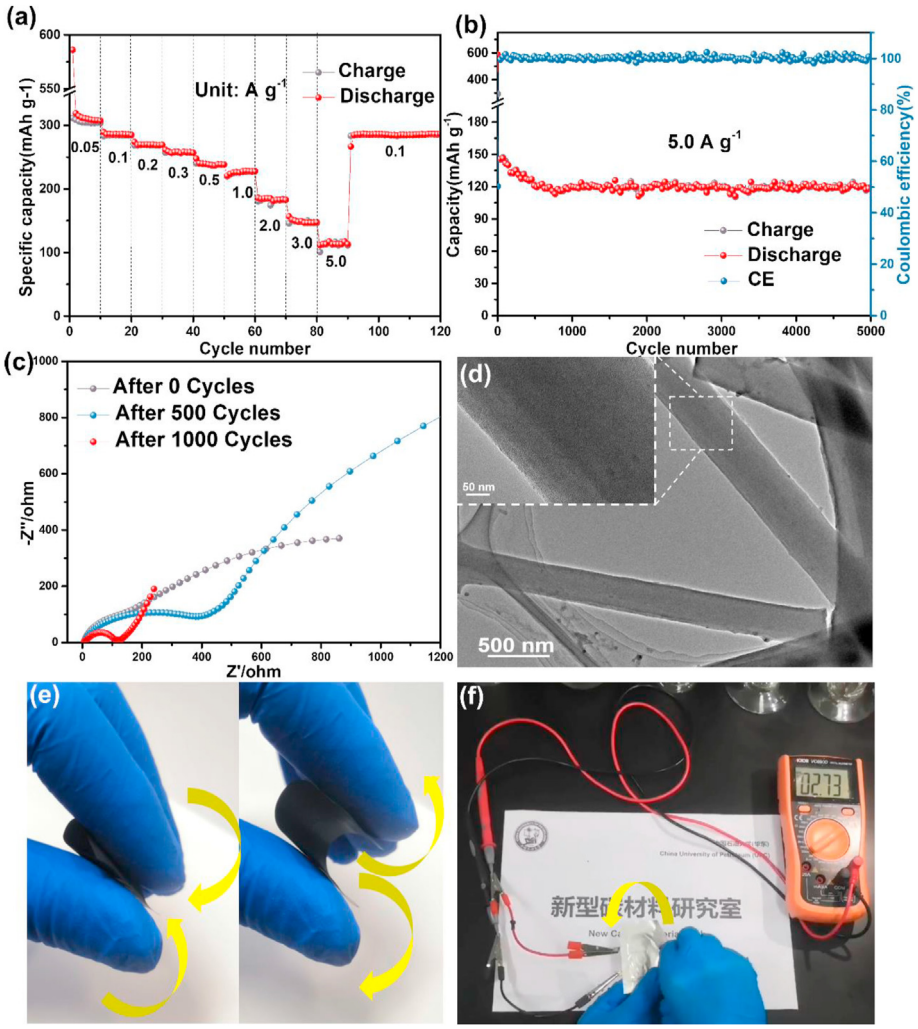

Fig. 7. (a) Rate capability of *uf*-Fe_3O_4@N-CNFs at different current densities. (b) Long cycling profiles of *uf*-Fe_3O_4@N-CNFs at a large current density of 5.0 A g^{-1}. (c) Nyquist impedance plots of *uf*-Fe_3O_4@N-CNFs after certain electrochemical cycles. (d) TEM image of *uf*-Fe_3O_4@N-CNFs after 1000 cycles at 1A g^{-1}. (e) Side view of the *uf*-Fe_3O_4@N-CNFs membrane. (f) Photograph of the flexible SIBs with optional bending. (A colour version of this figure can be viewed online.)

charge and discharge profiles of *uf*-TMOs@N-CNFs were also conducted at current densities from 0.05A g^{-1} to 5.0 A g^{-1}. As illustrated in Figs. S12–S14, the charge/discharge capacities decrease accordingly with increasing of the current density. Several slopes can be seen without obvious plateaus, which should be mainly associated with the discontinuous phase transition of the host material upon Na^+ insertion and extraction [46,47]. Moreover, the distance between the charge and discharge curves also increases with the current density, suggesting a gradually raised degree of polarization [48,49]. The long-term cycling performance of *uf*-Fe_3O_4@N-CNFs at a large current density was further investigated (Fig. 7b). In this process, the current density is initially set to be 5.0 A g^{-1}, and the structure of the electrode is inevitably damaged under such a large current density, resulting in a capacity fading in the initial cycles. Therefore, after a long activation procedure, which involves in the formation of stable SEI and ion/electron transmission channels, the capacity becomes stable and remains 119 mAh g^{-1} even after ultralong 5000 cycles.

Fig. 7c further illustrates the Nyquist impedance plots of *uf*-Fe_3O_4@N-CNFs after certain electrochemical cycles. The equivalent circuit and fitted curve (black dashed line) for *uf*-Fe_3O_4@N-CNFs after 1000 cycles are shown in Fig. S15. The fitted electrochemical impedance parameters listed in Table S7 indicates the good fitting degree of the equivalent circuit. For the Nyquist impedance plots, the semicircle at high-medium frequency reflects the charge-transfer resistance (R_{ct}) and Na^+ ions migration resistance through the SEI film (R_{SEI}). While the inclined line at low frequency corresponds to Warburg impedance (Zw) assigned from the diffusion of Na^+ ions into the electrodes [38]. Remarkably, the smaller semicircle diameter and higher slope of *uf*-Fe_3O_4@N-CNFs after 1000 cycles reveals a gradual activation behavior during the cycling process. Such activation phenomenon can be found in many TMOs-based electrodes, which should be partially attributed to the delayed wetting of the electrolyte into the composite, as well as gradually formed and aged transport channels for the Na^+ ions and electrons during the sodiation/desodiation processes, leading to promoted charge transfer and Na^+ diffusion kinetics [50–52]. Nyquist impedance measurements of *uf*-Fe_3O_4@N-CNFs, Fe_3O_4@N-CNFs, and Fe_3O_4 were further compared at a current density of 1 A g^{-1} after 20 cycles and 1000 cycles, as shown in Fig. S16. As can be seen, Fe_3O_4@N-CNFs and *uf*-Fe_3O_4@N-CNFs exhibit much smaller semicircle and higher slope than that of Fe_3O_4, indicating the enhanced electron and ion transportation by combination with carbonaceous substrates. After 1000 cycles, Fe_3O_4@N-CNFs shows severe fading of the electron and ion conductivity due to the structural damage of the electrode. Whereas *uf*-Fe_3O_4@N-CNFs

exhibits promoted charge transfer and Na^+ diffusion kinetics benefiting from the reinforced nanostructure and activation process. To further verify the structure change of the electrode, TEM images of *uf*-Fe_3O_4@N-CNFs after 1000 cycles at 1 A g^{-1} were detected and shown in Fig. 7d. Ultrafine Fe_3O_4 nanoparticles are firmly confined into continuous carbon nanofibers without any agglomeration or fracture, illuminating the prominent structural integrity during the repetitive cycling processes. As a control, TEM image of Fe_3O_4@N-CNFs shows the presence of irregular and agglomerated Fe_3O_4 particles on fractured nanofibers, which should be attributed to the severe volume change of Fe_3O_4 in the cycling process, resulting in pulverization and agglomeration of Fe_3O_4, as well as severe damage of the N-CNFs matrix (Fig. S17). Therefore, according to the above results, the excellent rate capability and durable ultralong cycling performance of *uf*-Fe_3O_4@N-CNFs are attributed to intimate interaction between ultrafine TMOs and conductive N-CNFs substrates, which can not only mitigate the volume changes of Fe_3O_4 during the sodiation/desodiation processes, but also shorten the solid-state diffusion paths of Na^+ and facilitate the electron/ion transfer.

Remarkably, the obtained *uf*-Fe_3O_4@N-CNFs membrane also exhibits excellent mechanical flexibility, which can sustain repeated buckling or folding (Fig. 7e). Considering the impressive flexibility, the *uf*-Fe_3O_4@N-CNFs was directly cut into rectangle pieces and assembled to a packaged flexible SIBs. As shown in Fig. 7f and Video S1, the output voltage does not show any change with optional bending of the flexible battery. Fig. S18 presents the cycling performance of the flexible battery with *uf*-Fe_3O_4@N-CNFs anode at a current density of 0.05 A g^{-1}. The electrode shows a stable cycling performance and delivers a high capacity of 297 mA h g^{-1} after 50 cycles. These results demonstrate the great potential of *uf*-Fe_3O_4@N-CNFs for application in flexible SIBs and other flexible energy storage devices.

To understand the sodium storage mechanism of *uf*-TMOs@N-CNFs, *uf*-Fe_3O_4@N-CNFs was selected as a typical sample and investigated in detail at different sweep-rates by CV tests (Fig. 8a). Notably, with increasing scan rate, the CV curves of *uf*-Fe_3O_4@N-CNFs are maintained nearly unvaried except for the enlarged area, indicating great potential for high-rate sodium storage [53]. There is a general agreement that the scan rate (v) and measured current (i) obey the following equation:

$$i = av^b \tag{1}$$

Where a is a constant, and b is decided upon the slope of the $\log(v)$–$\log(i)$ plots. The b value can unveil the charge storage mechanism. It is a diffusion-dominated Na^+ process when the b is 0.5. Whereas for an ideal surface-controlled capacitive process, b is equal to 1.0. As shown in Fig. 8b, a linear relationship between $\log(i)$ and $\log(v)$ is displayed, and the b values are calculated to be 0.892 (peak I) and 0.924 (peak II), which implies that the kinetics of *uf*-Fe_3O_4@N-CNFs are mainly pseudocapacitive processes. Furthermore, the pseudocapacitive (k_1v) and diffusion-controlled behavior ($k_2v^{1/2}$) at a fixed potential could be evaluated from the following equation:

$$i(V) = k_1v + k_2v^{1/2} \tag{2}$$

Accordingly, the pseudocapacitive-controlled contribution is calculated to be 78.69% for *uf*-Fe_3O_4@N-CNFs at 1.0 mV s^{-1} as demonstrated by the light blue area (Fig. 8c). Fig. 8d shows the percentages of pseudocapacitive contribution at different scan rates. The ratio of the capacitive contribution gradually improves from 61.79% to 78.69% with increased scan rates. These results suggest that the sodium-storage mechanism is mainly dominated by pseudocapacitive process, which is much faster than diffusion-controlled process [53]. In addition, as an important parameter to evaluate the kinetics for the electrochemical process, the sodium ion diffusion coefficient (D_{Na+}) was further calculated according to the above CV and electrochemical impedance spectroscopy (EIS) results. The detailed calculation method and results are listed in the supplementary information (Figs. S19–S21). Based on the CV

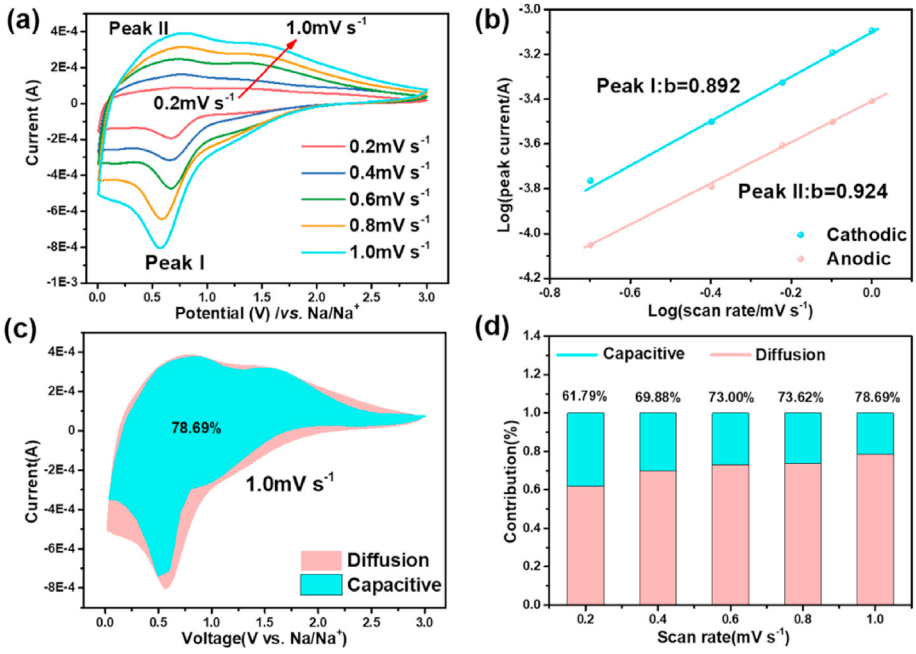

Fig. 8. Kinetics and quantitative analysis of the Na^+ storage behavior of *uf*-Fe_3O_4@N-CNFs anode: (a) CV curves at different scan rates. (b) Logarithm peak current versus logarithm scan rate plots. (c) Separation of capacitive (pink region) and diffusion-controlled (light blue region) contribution at 1.0 mV s^{-1}. (d) The percentages of pseudocapacitive contribution at different scan rates. (A colour version of this figure can be viewed online.)

results, the D_{Na+} of *uf*-Fe_3O_4@N-CNFs are calculated to be 1.97×10^{-12} and 7.22×10^{-12} cm^2 s^{-1} for the anodic and cathodic processes, respectively, which are of the same order with the D_{Na+} calculated by EIS (4.03×10^{-12} cm^2 s^{-1}) and superior to many reported TMOs-based materials [54–56]. Therefore, the high ion diffusion coefficient, as well as enhanced electron transfer and shortened ion diffusion pathways, are responsible for the boosted pseudocapacitive charge storage [47].

All of the above results indicate that the *uf*-TMOs@N-CNFs composites exhibit intriguing mechanical property and robust electrochemical sodium storage performances. With the formation of strong PVP-bonded-M^{n+} interaction, PVP is employed as an effective additive to disperse the metal precursors, suppress metal agglomeration, and control the formation kinetics of TMOs. Through downsizing of TMOs nanoparticles and strong interfacial interaction with the conductive N-CNFs substates, the fantastic nanostructure of *uf*-TMOs@N-CNFs composites endow them to mitigate the aggregation and pulverization of TMOs, facilitate electron/ion transfer, and boost pseudocapacitive charge storage in the charge/discharge processes. Satisfactory reversible capacity, excellent rate capability, and durable cycling stability are achieved. Remarkably, the excellent mechanical flexibility of *uf*-TMOs@N-CNFs also demonstrates their great potential for application in flexible energy storage devices.

4. Conclusion

In conclusion, we demonstrate a facile and general strategy to fabricate *uf*-TMOs@N-CNFs as robust and flexible anodes for SIBs. PVP is proved to be a crucial additive for the controllable synthesis of ultrafine TMOs nanoparticles intimately encapsulated in N-CNFs matrix. The intimate interaction between ultrafine TMOs and conductive N-CNFs substrates can efficiently mitigate the aggregation and pulverization of TMOs, facilitate electron/ion transfer, and boost pseudocapacitive charge storage, leading to superior sodium storage performance. For instance, the *uf*-Fe_3O_4@N-CNFs delivers a satisfactory capacity (234.5 mA h g^{-1} at 1 A g^{-1} after 1000 cycles with pseudocapacitive-controlled contribution of 78.69%), remarkable rate capability, and durable cycling stability (119.4 mAh g^{-1} at 5A g^{-1} after 5000 cycles). The excellent flexibility of *uf*-TMOs@N-CNFs also renders them great potential as anodes for flexible SIBs. We believe that the present work would provide a feasible and general method to construct ultrafine TMOs/carbon composites as advanced electrodes for renewable and flexible energy storage devices.

CRediT authorship contribution statement

Qingshan Zhao: Investigation, Conceptualization, Writing - review & editing, Funding acquisition. **Zhengzheng Xia:** Investigation, Methodology, Data curation, Writing - original draft. **Tong Qian:** Methodology, Data curation. **Xianchao Rong:** Formal analysis, Data curation. **Mei Zhang:** Data curation, Writing - original draft. **Yunfa Dong:** Formal analysis, Methodology. **Jinqing Chen:** Investigation, Data curation. **Hui Ning:** Methodology, Validation. **Zhongtao Li:** Resources, Project administration. **Han Hu:** Resources, Project administration. **Mingbo Wu:** Writing - review & editing, Supervision, Funding acquisition.

Declaration of competing interest

The authors declare that they have no known competing financial interests or personal relationships that could have appeared to influence the work reported in this paper.

Acknowledgements

This work was financially supported by the Shandong Provincial Natural Science Foundation (No. ZR2019QB016, ZR2018ZC1458), China; the National Natural Science Foundation of China (No. U1662113); the Fundamental Research Fund for the Central Universities (No. 18CX02015A, 15CX08005A), China; the Financial Support from Taishan Scholar Project of Shandong Province of China (No. ts201712020), China; Technological Leading Scholar of 10000 Talent Project (No. W03020508), China.

Appendix A. Supplementary data

Supplementary data to this article can be found online at https://doi.org/10.1016/j.carbon.2020.12.016.

References

[1] W. Liu, M.S. Song, B. Kong, Y. Cui, Flexible and stretchable energy storage: recent advances and future perspectives, Adv. Mater. 29 (1) (2017) 1–34.
[2] B. Dunn, H. Kamath, J.-M. Tarascon, Electrical energy storage for the grid: a battery of choices, Science 334 (6058) (2011) 928.
[3] J.B. Goodenough, Y. Kim, Challenges for rechargeable Li batteries, Chem. Mater. 22 (3) (2010) 587–603.
[4] V. Palomares, P. Serras, I. Villaluenga, K.B. Hueso, J. Carretero-González, T. Rojo, Na-ion batteries, recent advances and present challenges to become low cost energy storage systems, Energy Environ. Sci. 5 (3) (2012) 5884–5901.
[5] Y. Jiang, M. Hu, D. Zhang, T. Yuan, W. Sun, B. Xu, M. Yan, Transition metal oxides for high performance sodium ion battery anodes, Nanomater. Energy 5 (2014) 60–66.
[6] S.H. Yu, S.H. Lee, D.J. Lee, Y.E. Sung, T. Hyeon, Conversion reaction-based oxide nanomaterials for lithium ion battery anodes, Small 12 (16) (2016) 2146–2172.
[7] M.-S. Balogun, Y. Luo, W. Qiu, P. Liu, Y. Tong, A review of carbon materials and their composites with alloy metals for sodium ion battery anodes, Carbon 98 (2016) 162–178.
[8] T. Liu, Y. Zhang, Z. Jiang, X. Zeng, J. Ji, Z. Li, X. Gao, M. Sun, Z. Lin, M. Ling, J. Zheng, C. Liang, Exploring competitive features of stationary sodium ion batteries for electrochemical energy storage, Energy Environ. Sci. 12 (5) (2019) 1512–1533.
[9] J. Ji, Y. Li, W. Peng, G. Zhang, F. Zhang, X. Fan, Advanced graphene-based binder-free electrodes for high-performance energy storage, Adv. Mater. 27 (36) (2015) 5264–5279.
[10] S.-K. Jung, I. Hwang, D. Chang, K.-Y. Park, S.J. Kim, W.M. Seong, D. Eum, J. Park, B. Kim, J. Kim, J.H. Heo, K. Kang, Nanoscale phenomena in lithium-ion batteries, Chem. Rev. 120 (14) (2019) 6684–6737.
[11] M. Noked, C. Liu, J. Hu, K. Gregorczyk, G.W. Rubloff, S.B. Lee, Electrochemical thin layers in nanostructures for energy storage, Acc. Chem. Res. 49 (10) (2016) 2336–2346.
[12] C. Wu, Y. Jiang, P. Kopold, P.A. van Aken, J. Maier, Y. Yu, Peapod-Like carbon-encapsulated cobalt chalcogenide nanowires as cycle-stable and high-rate materials for sodium-ion anodes, Adv. Mater. 28 (33) (2016) 7276–7283.
[13] P. Chandra Rath, J. Patra, D. Saikia, M. Mishra, J.-K. Chang, H.-M. Kao, Highly enhanced electrochemical performance of ultrafine CuO nanoparticles confined in ordered mesoporous carbons as anode materials for sodium-ion batteries, J. Mater. Chem. 4 (37) (2016) 14222–14233.
[14] K. Zhang, F. Xiong, J. Zhou, L. Mai, L. Zhang, Universal construction of ultrafine metal oxides coupled in N-enriched 3D carbon nanofibers for high-performance lithium/sodium storage, Nanomater. Energy 67 (2020), 104222.
[15] Z. Qiang, Y.-M. Chen, B. Gurkan, Y. Guo, M. Cakmak, K.A. Cavicchi, Y. Zhu, B.D. Vogt, Cooperatively assembled, nitrogen-doped, ordered mesoporous carbon/iron oxide nanocomposites for low-cost, long cycle life sodium-ion batteries, Carbon 116 (2017) 286–293.
[16] G. Xia, L. Zhang, F. Fang, D. Sun, Z. Guo, H. Liu, X. Yu, General synthesis of transition metal oxide ultrafine nanoparticles embedded in hierarchically porous carbon nanofibers as advanced electrodes for lithium storage, Adv. Funct. Mater. 26 (34) (2016) 6188–6196.
[17] H. Liu, M. Jia, Q. Zhu, B. Cao, R. Chen, Y. Wang, F. Wu, B. Xu, 3D-0D graphene-Fe_3O_4 quantum dot hybrids as high-performance anode materials for sodium-ion batteries, ACS Appl. Mater. Interfaces 8 (40) (2016) 26878–26885.
[18] Q. Zhao, J. Liu, Y. Wang, W. Tian, J. Liu, J. Zang, H. Ning, C. Yang, M. Wu, Novel in-situ redox synthesis of Fe_3O_4/rGO composites with superior electrochemical performance for lithium-ion batteries, Electrochim. Acta 262 (2018) 233–240.
[19] Y. Zhu, X. Lv, L. Zhang, X. Guo, D. Liu, J. Chen, J. Ji, Liquid-solid-solution assembly of $CoFe_2O_4$/graphene nanocomposite as a high-performance lithium-ion battery anode, Electrochim. Acta 215 (2016) 247–252.
[20] J.S. Lee, O.S. Kwon, S.J. Park, E.Y. Park, S.A. You, H. Yoon, J. Jang, Fabrication of ultrafine metal-oxide-decorated carbon nanofibers for DMMP sensor

application, ACS Nano 5 (10) (2011) 7992–8001.
[21] X.L. Gao, Superdispersible PVP-coated Fe_3O_4 nanocrystals prepared by a "one-pot" reaction, J. Phys. Chem. B 112 (2008) 14390–14394.
[22] K.M. Koczkur, S. Mourdikoudis, L. Polavarapu, S.E. Skrabalak, Polyvinylpyrrolidone (PVP) in nanoparticle synthesis, Dalton Trans. 44 (41) (2015) 17883–17905.
[23] C. Liu, Y. Tan, Y. Liu, K. Shen, B. Peng, X. Niu, F. Ran, Microporous carbon nanofibers prepared by combining electrospinning and phase separation methods for supercapacitor, Journal of Energy Chemistry 25 (4) (2016) 587–593.
[24] T. Gong, R. Qi, X. Liu, H. Li, Y. Zhang, N, F-codoped microporous carbon nanofibers as efficient metal-free electrocatalysts for ORR, Nano-Micro Lett. 11 (1) (2019) 9.
[25] H. Pang, Z. Yang, J. Lv, W. Yan, T. Guo, Novel MnO_x@Carbon hybrid nanowires with core/shell architecture as highly reversible anode materials for lithium ion batteries, Energy 69 (2014) 392–398.
[26] H. Duan, S. Zhang, Z. Chen, A. Xu, S. Zhan, S. Wu, Self-formed channel boosts ultrafast lithium ion storage in Fe_3O_4@Nitrogen-doped carbon nanocapsule, ACS Appl. Mater. Interfaces 12 (1) (2020) 527–537.
[27] S. Zhang, W. Li, B. Tan, S. Chou, Z. Li, S. Dou, One-pot synthesis of ultra-small magnetite nanoparticles on the surface of reduced graphene oxide nanosheets as anodes for sodium-ion batteries, 2D Film 3 (9) (2015) 4793–4798.
[28] Y.-C. Lee, S.-Y. Hu, W. Water, Y.-S. Huang, M.-D. Yang, J.-L. Shen, K.-K. Tiong, C.-C. Huang, Improved optical and structural properties of ZnO thin films by rapid thermal annealing, Solid State Commun. 143 (4–5) (2007) 250–254.
[29] S. Mirzaee, S.F. Shayesteh, Ultrasound induced strain in ultrasmall $CoFe_2O_4$@polyvinyl alcohol nanocomposites, Ultrason. Sonochem. 40 (Pt A) (2018) 583–586.
[30] N. Al-Haj Husain, J. Camilleri, M. Ozcan, Effect of polishing instruments and polishing regimens on surface topography and phase transformation of monolithic zirconia: an evaluation with XPS and XRD analysis, J Mech Behav Biomed Mater 64 (2016) 104–112.
[31] Y. Zhao, F. Wang, C. Wang, S. Wang, C. Wang, Z. Zhao, L. Duan, Y. Liu, Y. Wu, W. Li, D. Zhao, Encapsulating highly crystallized mesoporous Fe_3O_4 in hollow N-doped carbon nanospheres for high-capacity long-life sodium-ion batteries, Nanomater. Energy 56 (2019) 426–433.
[32] J. Zhu, C. Chen, Y. Lu, Y. Ge, H. Jiang, K. Fu, X. Zhang, Nitrogen-doped carbon nanofibers derived from polyacrylonitrile for use as anode material in sodium-ion batteries, Carbon 94 (2015) 189–195.
[33] Y. Zuo, G. Wang, J. Peng, G. Li, Y. Ma, F. Yu, B. Dai, X. Guo, C.-P. Wong, Hybridization of graphene nanosheets and carbon-coated hollow Fe_3O_4 nanoparticles as a high-performance anode material for lithium-ion batteries, J. Mater. Chem. 4 (7) (2016) 2453–2460.
[34] J. Ming, H. Ming, W. Yang, W.-J. Kwak, J.-B. Park, J. Zheng, Y.-K. Sun, A sustainable iron-based sodium ion battery of porous carbon–Fe_3O_4/$Na_2FeP_2O_7$ with high performance, RSC Adv. 5 (12) (2015) 8793–8800.
[35] D. Pham-Cong, S.J. Kim, S.Y. Jeong, J.-P. Kim, H.G. Kim, P.V. Braun, C.-R. Cho, Enhanced cycle stability of iron(II, III) oxide nanoparticles encapsulated with nitrogen-doped carbon and graphene frameworks for lithium battery anodes, Carbon 129 (2018) 621–630.
[36] Q. Tan, P. Li, K. Han, Z. Liu, Y. Li, W. Zhao, D. He, F. An, M. Qin, X. Qu, Chemically bubbled hollow Fe_xO nanospheres anchored on 3D N-doped few-layer graphene architecture as a performance-enhanced anode material for potassium-ion batteries, J. Mater. Chem. 7 (2) (2019) 744–754.
[37] X.Y. Chen, B.H. Liu, Z.P. Li, Fe_3O_4/C composites synthesized from Fe-based xerogels for anode materials of Li-ion batteries, Solid State Ionics 261 (2014) 45–52.
[38] Q. Zhao, J. Liu, X. Li, Z. Xia, Q. Zhang, M. Zhou, W. Tian, M. Wang, H. Hu, Z. Li, W. Wu, H. Ning, M. Wu, Graphene oxide-induced synthesis of button-shaped amorphous Fe_2O_3/rGO/CNFs films as flexible anode for high-performance lithium-ion batteries, Chem. Eng. J. 369 (2019) 215–222.
[39] D. Li, J. Zhou, X. Chen, H. Song, Amorphous Fe_2O_3/graphene composite nanosheets with enhanced electrochemical performance for sodium-ion battery, ACS Appl. Mater. Interfaces 8 (45) (2016) 30899–30907.
[40] L.-Y. Qi, Y.-W. Zhang, Z.-C. Zuo, Y.-L. Xin, C.-K. Yang, B. Wu, X.-X. Zhang, H.-H. Zhou, In situ quantization of ferroferric oxide embedded in 3D microcarbon for ultrahigh performance sodium-ion batteries, J. Mater. Chem. 4 (22) (2016) 8822–8829.
[41] J. Liu, X. Xu, R. Hu, L. Yang, M. Zhu, Uniform hierarchical Fe_3O_4@Polypyrrole nanocages for superior lithium ion battery anodes, Adv. Energy Mater. 6 (13) (2016), 1600256.
[42] L. Chen, X. Guo, W. Lu, M. Chen, Q. Li, H. Xue, H. Pang, Manganese monoxide-based materials for advanced batteries, Coord. Chem. Rev. 368 (2018) 13–34.
[43] Y. Zhou, W. Sun, X. Rui, Y. Zhou, W.J. Ng, Q. Yan, E. Fong, Biochemistry-derived porous carbon-encapsulated metal oxide nanocrystals for enhanced sodium storage, Nanomater. Energy 21 (2016) 71–79.
[44] Y. Teng, M. Mo, Y. Li, J. Xue, H. Zhao, Amorphous carbon-coated ZnO porous nanosheets: facile fabrication and application in lithium- and sodium-ion batteries, J. Alloys Compd. 744 (2018) 712–720.
[45] T. Wang, H. Li, S. Shi, T. Liu, G. Yang, Y. Chao, F. Yin, 2D film of carbon nanofibers elastically astricted MnO microparticles: a flexible binder-free anode for highly reversible lithium ion storage, Small 13 (20) (2017), 1604182.
[46] G.A. Muller, J.B. Cook, H.S. Kim, S.H. Tolbert, B. Dunn, High performance pseudocapacitor based on 2D layered metal chalcogenide nanocrystals, Nano Lett. 15 (3) (2015) 1911–1917.
[47] K. Zhao, F. Liu, C. Niu, W. Xu, Y. Dong, L. Zhang, S. Xie, M. Yan, Q. Wei, D. Zhao, L. Mai, Graphene oxide wrapped amorphous copper vanadium oxide with enhanced capacitive behavior for high-rate and long-life lithium-ion battery anodes, Adv. Sci. 2 (12) (2015), 1500154.
[48] Y. Liu, L. Zhang, D. Liu, W. Hu, X. Yan, C. Yu, H. Zeng, T. Shen, Turbostratic carbon-localised FeS_2 nanocrystals as anodes for high-performance sodium-ion batteries, Nanoscale 11 (33) (2019) 15497–15507.
[49] S.H. Park, W.J. Lee, Hierarchically mesoporous CuO/carbon nanofiber coaxial shell-core nanowires for lithium ion batteries, Sci. Rep. 5 (2015) 9754.
[50] H.B. Wu, J.S. Chen, H.H. Hng, X.W. Lou, Nanostructured metal oxide-based materials as advanced anodes for lithium-ion batteries, Nanoscale 4 (8) (2012) 2526–2542.
[51] R. Chu, D. Tan, J. Zhang, Y. Chen, H. Jiang, J. Lin, L. Li, Y. Zhang, H. Guo, Long-term cycling of core-shell Fe_3O_4-Polypyrrole composite electrodes via diffusive and capacitive lithiation, J. Alloys Compd. 835 (2020), 155192.
[52] M. Xu, Q. Xia, J. Yue, X. Zhu, Q. Guo, J. Zhu, H. Xia, Rambutan-Like hybrid hollow spheres of carbon confined Co_3O_4 nanoparticles as advanced anode materials for sodium-ion batteries, Adv. Funct. Mater. 29 (6) (2019), 1807377.
[53] N. Wang, Q.L. Liu, Y. Li, J.C. Chen, J.J. Gu, W. Zhang, D. Zhang, Self-crosslink assisted synthesis of 3D porous branch-like Fe_3O_4/C hybrids for high-performance lithium/sodium-ion batteries, RSC Adv. 7 (79) (2017) 50307–50316.
[54] H. Mi, Y. Wang, H. Chen, L. Sun, X. Ren, Y. Li, P. Zhang, Boosting Na-ion diffusion by piezoelectric effect induced by alloying reaction of micro red-phosphorus/BaTiO3/graphene composite anode, Nanomater. Energy 66 (2019), 104136.
[55] G. Ali, M. Islam, J.Y. Kim, H.G. Jung, K.Y. Chung, Kinetic and electrochemical reaction mechanism investigations of rodlike $CoMoO_4$ anode material for sodium-ion batteries, ACS Appl. Mater. Interfaces 11 (4) (2019) 3843–3851.
[56] B. Shang, Q. Peng, X. Jiao, G. Xi, X. Hu, Carbon nanotubes enhanced Sb_6O_{13} as a new anode material for sodium-ion batteries, Ionics 25 (2) (2019) 523–531.